Article:
Wingham, J.R., Turner, R., Shepherd, J. et al. (2020) Micro-CT for analysis of laser sintered micro-composites. Rapid Prototyping Journal, 26 (4). pp. 649-657. ISSN: 1355-2546

https://doi.org/10.1108/rpj-08-2019-0211

Micro-CT for analysis of Laser Sintered micro-composites

Abstract

Purpose – X-Ray Computed Micro-Tomography (Micro-CT) is relatively well established in Additive Manufacturing as a method to determine the porosity and geometry of printed parts, and in some cases the presence of **inclusions or contamination**. This paper demonstrates that micro-CT can be also be used to quantitatively analyse the homogeneity of micro-composite parts, in this case created using Laser Sintering (LS).

Design/methodology/approach – LS specimens were manufactured in polyamide 12, with and without incorporation of a silver phosphate glass additive in different sizes. The specimens were scanned using micro-CT to characterise both their porosity and the homogeneity of dispersion of the additive throughout the volume.

Findings – This work showed that it was possible to use micro-CT to determine information related to both porosity and additive dispersion from the same scan. Analysis of the pores revealed the overall porosity of the printed parts, with linear elastic fracture mechanics used to identify any pores likely to lead to premature failure of the parts. Analysis of the additive was found to be possible above a certain size of particle, with the size distribution used to identify any agglomeration of the silver phosphate glass. The particle positions were also used to determine the complete spatial randomness of the additive as a quantitative measure of the dispersion.

Practical implications – This shows that micro-CT is an effective method of identifying both porosity and additive agglomeration within printed parts, meaning it can be used for quality control of micro-composites and to validate the homogeneity of the polymer/additive mixture prior to printing.

Originality/value – This is believed to be the first instance of micro-CT being used to identify and analyse the distribution of an additive within a Laser Sintered part.

Keywords: Laser Sintering, Micro-Composite, Computed Tomography, Non-Destructive Testing, Quality Control, Microstructure

1. Introduction

Additive Manufacturing (AM), more commonly referred to as 3D printing, is a term encompassing a family of processes which join materials, usually layer by layer, to make parts from 3D model data (ASTM, 2015). In recent years, there has been a move towards the manufacture of end-use components (rather than prototypes) using these techniques, a move which has been accompanied by a greater need to understand material properties and establish suitable quality control methods (Wohlers *et al.*, 2018a). Laser Sintering (LS) is a well established AM process which has increasingly been used for the production of functional products; this technique uses a laser to selectively melt consecutive cross-sections of a material in a powder bed. Primarily used for polymers, LS is particularly suited to the production of end-use parts due to its relatively high mechanical properties, along with the complex geometries and assemblies possible due to the ability of the un-sintered powder to act as a supports (Goodridge *et al.*, 2012; Schmidt *et al.*, 2017).

Boosted by the push towards production of functional parts, the range of materials available for LS is increasing rapidly (Wohlers *et al.*, 2018b); with new machines capable of processing a wide variety of polymers. As well as the choice of base polymer, added functionality and increased mechanical properties can be achieved by the inclusion of additives (or fillers). The additives used in these nano- and micro-composite materials are not generally melted by the laser, instead they are incorporated into the part by melting of the surrounding polymer (Kruth *et al.*, 2007). As with any composite, the distribution of its component materials can have a large effect on the performance of the part as a whole. While methods of determining this distribution exist, these have generally either been surface techniques, or involved destruction of the part. For example, whilst cutting a cross sectional slice from a part and inspecting it using microscopy can provide an accurate analysis, it is limited to the section analysed and the component is no longer functional. For production parts, this is not ideal, as it is often beneficial to carry out quality control (QC) checks on the actual parts prior to use; a non-destructive testing technique is therefore preferable for this type of application.

X-Ray Computed Micro-Tomography (Micro-CT) is a non-destructive 3D imaging technique capable of analysing the internal and external geometry of complex components. This is now widely used as a method to examine the porosity of AM parts (Thompson *et al.*, 2016) and has been described as the only technique capable of industrial QC of internal features created with AM (Chiffre *et al.*, 2014). However, micro-CT has the potential to be used for far more than is presently done, for example seeing particles in printed parts (du Plessis *et al.*, 2018; Dzogbewu *et al.*, 2017). The basic principle is shown in Figure 1, where multiple 2D x-ray images are taken through the side of a component at varying angles; these images are then reconstructed

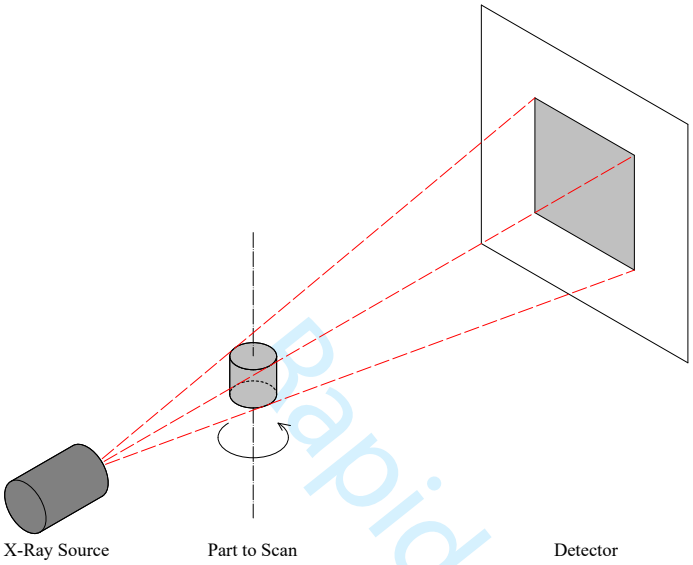

Figure 1: Schematic diagram of Micro-CT.

into an image stack of top-down views through the thickness of the part, which can then be used for analysis.

The majority of recent literature on micro-CT in AM has focused around metals (Thompson *et al.*, 2016); however, studies using polymer LS have also utilised this approach to measure porosity and geometry. Polyamide 12 (PA12) is the most widely used material for LS and is the most well documented for use with micro-CT. Other polymeric materials have also been analysed using this process, such as PEK (Ghita *et al.*, 2014), PEEK (Berretta *et al.*, 2015) and, in some instances, micro-composite materials (Jansson and Pejryd, 2016); however, in all cases the analysis has been focused solely on the porosity and geometry of the parts.

For the literature based on PA12, the use of micro-CT has evolved from simply a qualitative technique for viewing pores within the part (Rüsenberg *et al.*, 2011; Dupin *et al.*, 2012), into a more sophisticated method of determining the porosity (Rouholamin and Hopkinson, 2014), pore size (Stichel *et al.*, 2018; Pavan *et al.*, 2018) and pore distribution within the parts (Dewulf *et al.*, 2016; Pavan *et al.*, 2017, 2016); alongside geometry measurements (Pavan *et al.*, 2016). Despite these advances, there are still large discrepancies both in terms of the analyses carried out and the final data presented, often with essential values required for comparing analyses omitted. The information-rich data from the scanning can still be exploited to a greater extent, without the need for any further experimental work. For example quantitative metrics for measuring internal feature morphology and spatial distribution are relatively underused.

For most uses in AM, the contrast of part-air is the most important, as this can be used to compare the external geometry to the 3D model, and to analyse internal features such as porosity. However, the ability to distinguish between multiple materials with sufficiently different densities / chemical compositions is also possible; with micro-CT occasionally used to detect **inclusions /** contamination within an AM part **(du Plessis *et al.*, 2015, 2018; du Plessis and le Roux, 2018), or within the material feedstock (du Plessis *et al.*, 2016)**. To the authors' knowledge, the only instance where different materials inside composite AM parts have been identified can be found in metal AM (Chlebus *et al.*, 2015; Dzogbewu *et al.*, 2017), where micro-CT has been used to identify unmelted particles in titanium alloys (namely Rhenium and Molybdenum). These studies provided a qualitative visual indication of the particle positions, without explicitly carrying out any quantitative analysis.

Figure 2: Photo of the specimens printed for micro-CT scanning, showing (left to right) virgin PA2200, 1% B65003 and 1% B45003.

It is therefore clear that micro-CT can be a powerful tool for analysis of micro-composite materials, as it has the ability to identify individual additive particles. This paper presents a worked example of how to maximise the information obtained from a single micro-CT scan, whilst ensuring the accuracy of the results obtained.

2. Specimens and Scanning

2.1. *Materials*

In order to minimise the potential for scanning artefacts (ASTM, 2011), cylindrical specimens measuring 5×5 mm (D×L) were created for scanning; these were Laser Sintered on an EOS Formiga P100. The base polymer was a polyamide 12 powder (PA2200), with two silver phosphate glass additives (B45003 and B65003 – BioCote); these differed only in size, with diameters of $<10\,\mu$m and $<40\mu$m for B45003 and B65003 respectively. Test specimens were created from virgin (unused) PA2200, virgin PA2200 with 1.0% B45003 w/w, and virgin PA2200 with 1.0% B65003 w/w; the materials were mixed in a rotary tumbler for approximately 100 minutes. The builds carried out were identical for each material, with the cylinders oriented vertically and positioned in the centre of the build. The settings for printing were, laser power 21 W, scan spacing 0.25 mm, scan speed 2500 mm/s, with no contours; loose powder was removed from the printed parts using compressed air only. A photo of the printed parts can be seen in Figure 2.

2.2. *Micro-CT Scanning*

To analyse the dispersion of the additive and porosity within the micro-composites, the parts were scanned using a Skyscan 1172

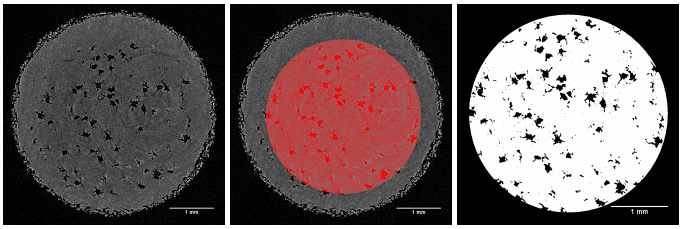

(a) PA2200.

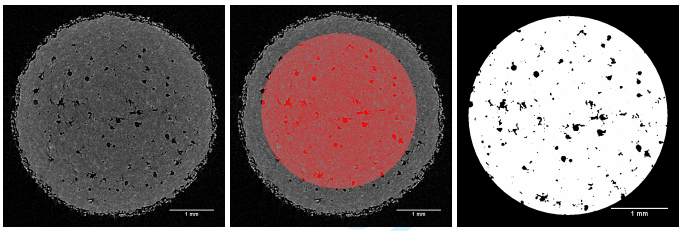

(b) 1.0% B45003.

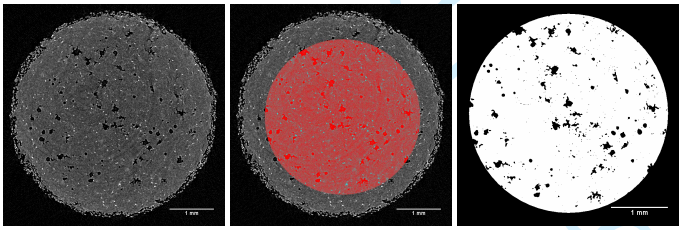

(c) 1.0% B65003.

Figure 3: Example slices of the data from Micro-CT scanning. Showing (left to right), the reconstructed slice, ROI (shown in red), and pores (shown in black).

MicroCT Scanner. The parameters used were, voltage 40 kV, current 144 µA, no filter, reconstructed voxel size 4.87 µm, rotation 180°, rotation step 0.35°, and a total scan time of 18 minutes; the detector resolution was 4000×2000 pixels (binned to 2000×1024). For these parameters, the voltage and filter affect the ability of the x-ray beam to penetrate the sample; whereas the pixel size, rotation and rotation step affect the quality and clarity of the reconstructed data. The settings used here were selected based on previous optimisation for a similar geometry and material.

3. Porosity Measurement

3.1. Reconstruction and Thresholding

In order to analyse the microstructure of the parts, the scan data first had to be processed into a suitable form. This comprised of three steps, namely reconstruction of the raw data, selection of a region of interest (ROI), and applying a threshold to the greyscale image to obtain a binarised value. An example cross-sectional slice for each material is presented in Figure 3 at each of these stages.

The scan data were reconstructed in NRecon, with a contrast setting of 0 – 0.35 used to differentiate between PA2200 (part) and air (pores). The region of interest (ROI) was defined as a 3.5×2.5 mm (D×L) cylinder positioned in the centre of the specimen. The last step shown in Figure 3 was to apply a threshold to the ROI in each case; this was determined visually by the operator and varied depending on the focus of the analysis.

To analyse the individual pores, a threshold of 0 – 35 was applied to identify the pores as features. To remove any noise from the scan data, a sweep was carried out to remove detected features <8 voxels in size. The value of 8 voxels is commonly used as it represents a 2×2×2 cube; another less common but equally valid value to use is 27 voxels (3×3×3) which eliminates even more features from the analysis (Pavan *et al.*, 2016; du Plessis *et al.*, 2018). **This criteria depends on the scan quality and noise levels. The combination of low-density parts and high scan quality used in this study resulted in low levels of noise, meaning that the smaller number of voxels could be used reliably.**

3.2. Pore Size Distribution

The porosity analysis was carried out using CTAn, with the volume (V_{actual}), major diameter (d_{maj} – the maximum distance between opposite walls) and surface area (A_{actual}) of each pore measured. The volume equivalent diameter (d_{vol}) was calculated from the measured volume using Equation 1; this was used to quantify the size of the features.

$$V_{\text{Sphere}} = \frac{4}{3}\pi\left(\frac{d_{\text{vol}}}{2}\right)^3 \quad \Rightarrow \quad d_{\text{vol}} = 2\left(\frac{3V_{\text{actual}}}{4\pi}\right)^{\frac{1}{3}} \tag{1}$$

The results of the porosity analysis are shown in Figure 4, with all materials showing similar results. The measured values of d_{vol} are shown, with the overall porosity values (determined by summing all the values of d_{vol}) found to be 4.9%, 4.7% and 4.6% for the 1% B65003, 1% B45003 and Virgin PA2200 respectively.

3.3. Pore Morphology

In this paper, the sphericity (ψ) was used as the single metric to describe the feature morphology due to its simplicity. Other values including orientation, presence of trapped powder, and connectivity could also be chosen if more detail was required. The value of ψ was calculated from A_{actual} and the surface area of the volume equivalent sphere (A_{vol}) using Equation 2.

$$\psi = \frac{A_{\text{vol}}}{A_{\text{actual}}} = \frac{\pi {d_{\text{vol}}}^2}{A_{\text{actual}}} = \frac{\sqrt[3]{\pi}(6V_{\text{actual}})^{\frac{2}{3}}}{A_{\text{actual}}} \tag{2}$$

The measured sphericity (ψ) of the pores was found to relate to the major pore diameter (d_{maj}), with larger pores being less spherical. This is shown in Figure 5, where the relationship of ψ and d_{maj} is shown. **For smaller pore sizes (those approaching the minimum detectable feature size), partial volume effects are likely to contribute to this trend, with the resolution of the scan creating an artificial smoothing effect.** The reason for showing the major diameter of the pores, rather than the volume equivalent diameter, is due to the likely impact on the mechanical properties of the part. The pores within the parts can be approximated to act as cracks, meaning that the maximum (or major) diameter of the pore gives a value equivalent to the crack length; this is explored further in Section 3.4.

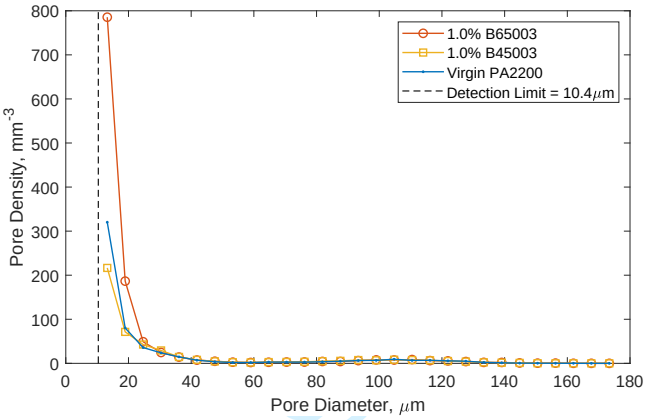

(a) Diameter by density of pores.

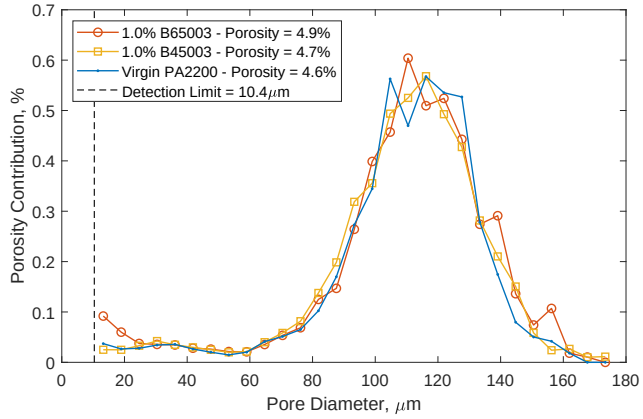

(b) Diameter by volume contribution.

Figure 4: Pore volume equivalent diameters for Virgin PA2200, 1.0% B45003, and 1.0% B65003. Here it can be seen that there is no significant difference in the porosity distributions for any of the tested materials.

3.4. *Critical Pore Size*

To determine whether the pore size was likely to have an impact on the mechanical properties of the printed parts, Linear Elastic Fracture Mechanics (LEFM) was used; a method which has been previously used for similar applications (Stichel *et al.*, 2018). For this, the pores were assumed to behave as embedded cracks in a plate of infinite dimensions. The critical crack size (a_c) could then be calculated using Equation 3 (Meyers and Chawla, 2009) and could be compared to d_{maj}, to determine whether this presents an issue.

$$K_{Ic} = Y\sigma_f\sqrt{a_c\pi} \quad \Rightarrow \quad a_c = \frac{1}{\pi}\left(\frac{K_{Ic}}{Y\sigma_f}\right)^2 \tag{3}$$

In Equation 3, K_{Ic} is the critical stress intensity factor for a mode I crack in the case of plane strain, Y is the calibration function accounting for the crack geometry, and σ_f is the stress at fracture. The value of Y will vary depending on the exact geometry of each pore. While this is possible to obtain this from micro-CT data, a value of $Y = 1$ has been used here representative of a through thickness crack; in reality, the rounded edges of

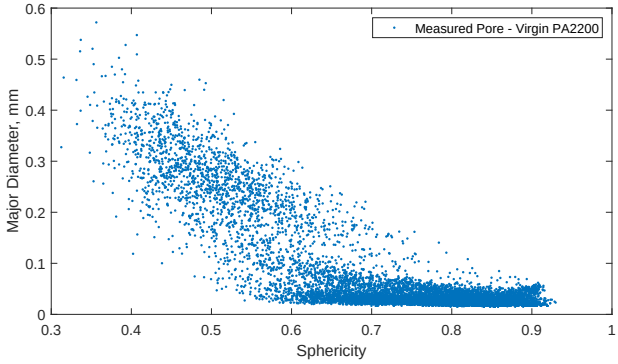

(a) Virgin PA2200.

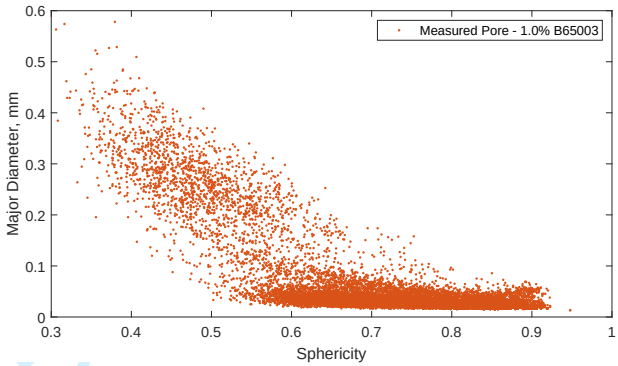

(b) 1% B65003.

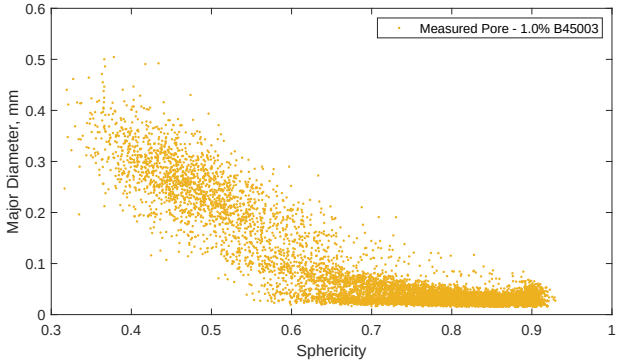

(c) 1% B45003.

Figure 5: Relationship of Sphericity (ψ) and major pore diameter (d_{maj}). It can be seen that for all measured pores, there appears to be a negative correlation between the major diameter and the sphericity of the pores.

the pores mean this is likely to be lower and this is simulating the "worst case" scenario. The value of K_{Ic} can be determined experimentally for a given material, in this instance a value of $K_{Ic} = 3.25\,\text{MPa}\sqrt{\text{m}}$ was chosen, which was previously measured as the most critical value of K_{Ic} in LS PA2200 parts (Brugo *et al.*, 2016). The stress at fracture has been arbitrarily chosen to be 40 MPa, a value slightly lower than the measured yield stress of the material, meaning that it represents a premature failure of the part in the elastic region. Using Equation 3, a critical crack length (a_c) of 2.1 mm was found, relating to a critical pore diameter (d_c) of 4.2 mm.

While this method provides an initial estimate of the effects on the mechanical properties, the positioning and proximity of the pores to one another will also have an effect. In order to accurately account for this, more detailed studies (such as the one carried out by Jones *et al.* (2009)) would have to be performed based on the actual geometry derived from the scan data.

3.5. Discussion

The distribution of measured pore sizes (shown in Figure 4), show that the pore sizes which contribute the highest amount to the overall porosity are those between 60 - 160 µm; both this, and the total porosity (4.9%), were found to be consistent with previous studies focused on pure PA2200 (Stichel *et al.*, 2018; Rouholamin and Hopkinson, 2014). The measured sphericity (ψ – shown in Figure 5), indicates that the smaller pores are more spherical. While it is likely that this is the case, it is worth noting that for small features, the smoothing effect of the surface fitting algorithm **(the partial volume effect)** could be artificially increasing this value (Lorensen and Cline, 1987). This effect will decrease with larger features, but if analysing very small features (in terms of number of voxels) such as the included additives, cannot be ignored. It is also worth noting, that should a more in depth analysis of the porosity be required, a smaller voxel size could be used to obtain a more accurate result.

The relationship of ψ vs d_{maj} (shown in Figure 5), reinforces the importance of detecting larger pores as they are more likely to act as crack initiators. The reason for this is twofold and can be explained using the LEFM in Section 3.4. Firstly, a larger d_{maj} is more likely to approach d_c. Secondly, the lower value of sphericity could mean a less rounded pore, effectively increasing the value of Y as the pore elongates, causing it to act more as a linear crack. Visually, this means that the pores appearing in the top left portion of Figure 5 pose the largest risk of acting as crack initiators. However, the largest measured value of d_{maj} was 0.58 mm and as $d_{\text{maj}} \ll d_c$, the measured pore sizes are unlikely to lead to fast fracture of the part within the elastic region.

4. Additive Distribution

4.1. Reconstruction and Thresholding

To distinguish between PA2200 and the additive, the scan data were processed in a similar manner to Section 3.1, using a contrast setting of 0 – 0.1 for the reconstruction; and a threshold of 60 – 255 to identify the brighter voxels as features and obtain the binary images. Figure 6 shows example binarised data (the same slices shown Figure 3) focusing on the additive.

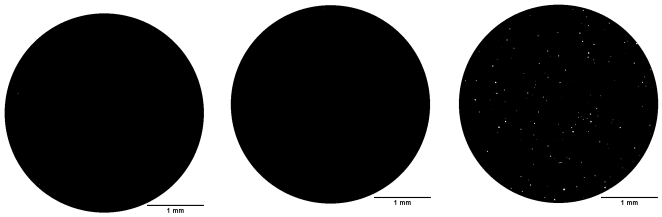

(a) PA2200. (b) 1.0% B45003. (c) 1.0% B65003.

Figure 6: Example slices of the reconstructed and binarised data, showing the additive (in white) within the ROI. Here it can be seen that with the same post-processing, features were only identified for 1.0% B65003 (Figure 6c).

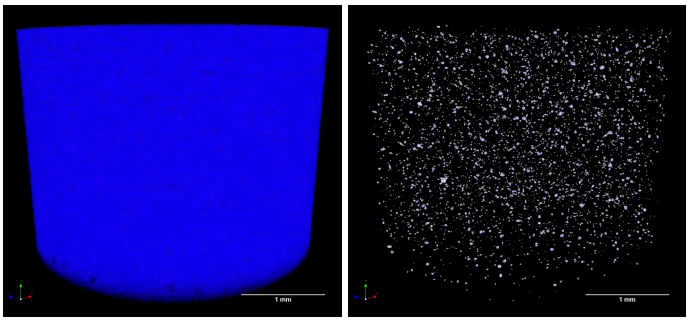

(a) PA2200 shown in blue. (b) Additive shown in grey.

Figure 7: 3D views of 1.0% B65003 scan data.

A 3D view of the scan data was created using CTvox to visualise the dispersion; this is shown in Figure 7, where the ROI is shown both with and without the base polymer. From this, it can be seen that the voxel size was too large to identify the additive for the 1.0% B45003 (Figure 6b), which had a particle size of $<10\,\mu\text{m}$.

From the 3D views of the data, a preliminary visual inspection of the additive was carried out. While the majority of particles appeared to be well dispersed, there were two larger "clumps" identified; one of these is shown for reference in Figure 8, both in the 2D reconstructed slice data and a 3D view.

While these initial observations provide a qualitative indication as to the dispersion, further analysis was performed to obtain a quantitative measurement of the part microstructure.

4.2. Additive Analysis

An individual object analysis was carried out on the binarised image, with the volume and positional data of each particle recorded. The analysis software used the marching cubes algorithm (Bruker, 2018) to determine volume, making the smallest detectable feature (8 voxels) approximately 10.3 µm in diameter for the chosen pixel size. **This value represents the volume equivalent diameter of a smoothed 2×2×2 voxel cube (Lorensen and Cline, 1987).**

The individual particle diameters (d_{vol}) were determined in the

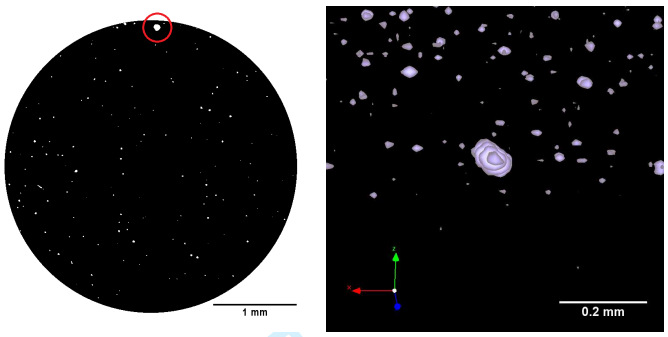

(a) Binarised 2D slice. (b) 3D view.

Figure 8: Views of a "clump" of additive as identified from an initial visualisation of the scan data.

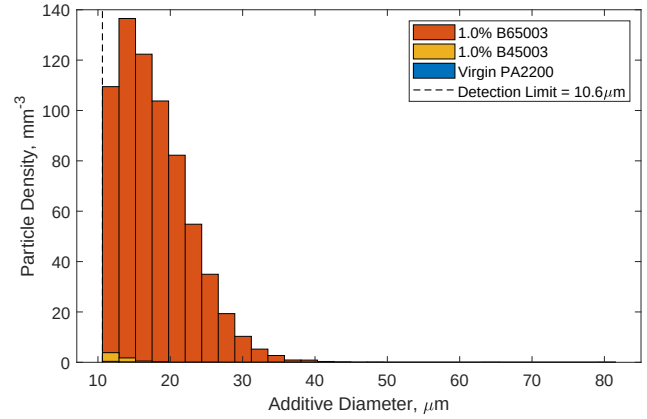

(a) Diameter by density of particles.

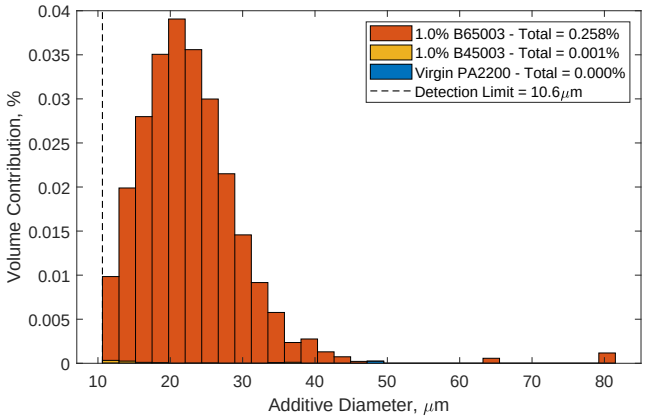

(b) Diameter by volume contribution.

Figure 9: Additive volume equivalent diameters for Virgin PA2200, 1.0% B45003, and 1.0% B65003.

part using the method in Section 3.2; these could then be compared to the pre-printed manufacturer's specifications (diameter <40 µm) to determine whether coalescence occurred. The distribution of d_{vol} for the additive in each scan is shown in Figure 9; the data for each material have been superimposed onto the same graph so that a direct comparison is possible.

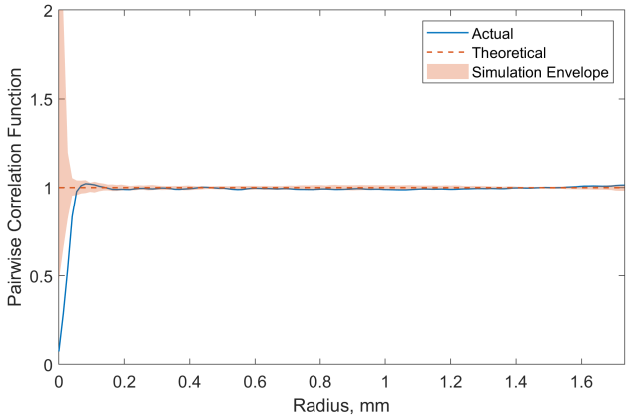

Figure 10: Complete Spatial Randomness (CSR) results for 1.0% B65003.

4.3. *Spatial Analysis*

In order to determine whether the additive particles within the parts were randomly distributed, the individual particle centroids were analysed for Complete Spatial Randomness (CSR), which measures the distances of every point from every other point and compares them to a simulated randomly distributed dataset. The resulting pairwise correlation function was determined using the `spatstat` *R* package function `pcf3est` (Baddeley *et al.*, 1993). This was compared to the theoretical value (1 for a perfect distribution), as well as a simulated envelope of CSR results obtained by simulating 99 random distributions with a similar number of points and the same dimensions as the experimental data.

For the additive spatial analysis, a comparison was plotted (Figure 10) revealing that at length scales above about 90 µm the distribution of additive particles conforms to CSR – the plot is close to the theoretical value and within the simulation envelope. At shorter length scales the line for experimental data falls below the simulation envelope. We propose that this is due to the physical size of the additive particles (and the PA2200 grains) making it impossible for centroids to be closer than a threshold value (of around the particle diameter).

4.4. *Discussion*

The scan parameters for both the additives analysed were kept the same throughout. For the larger additive (B65003), a high number of small particles were identified (Figure 9a) suggesting that there could be a large number of smaller particles which remained undetected. However, when compared with the volume contributions (Figure 9b), it can be seen that although these smaller particles may be many in number, the volume contribution of these smaller particles is small. Since detecting the presence of clumping and the dispersion of the majority of the additive throughout the part was of greatest interest, the voxel size was deemed to be sufficient for the analysis. On the other hand, the smaller additive (B45003) again showed a larger density of smaller particles, but the volume distribution did not appear to encapsulate the entire volume (which was expected to be similar in total volume to that of B65003), a smaller voxel size would therefore be required for

this analysis.

To ensure that the analysis was actually detecting the additive, rather than some other feature in the material, the same analysis was run on a pure PA2200 sample (also shown in Figure 9). A small number of features were detected with this, which are expected to be flow-enhancing additives included in the powder by the manufacturer (Goodridge *et al.*, 2012; Dupin *et al.*, 2012). As these detected features were small in number and volume, the analysis was deemed to be valid.

An advantage of plotting the sizes by volume, rather than by number, was the ability to easily identify any agglomeration of the additive. The two peaks in Figure 9b present at $\approx 64\,\mu m$ and $\approx 81\,\mu m$ correspond to two "clumps" which were previously observed (the latter is shown in Figure 8). This volume distribution will also be independent of the voxel size used (provided the scan data is of sufficient quality), as frequency distributions can be deceptively weighted towards a large number of small particles.

From the spatial analysis, the key finding was that above 90 µm all the particles were randomly distributed. This means that all the properties affected by the additive distribution are also likely to be uniform above this length scale.

5. Conclusion

This paper has shown that it is possible to obtain quantitative metrics for the porosity and additive dispersion from the same part, using the same scan data. Analyses of the porosity, such as the size and sphericity of individual pores, were used to identify potential stress-raisers capable of causing premature part failure; whereas size and spatial analyses of the additive were used to identify clumps and determine the uniformity of the dispersion, both indicative signs of ineffective mixing. This research has shown that micro-CT is an effective method to assess the microstructure of micro-composite parts, capable of quantitative analysis of both the pores and additives.

References

ASTM (2011), "ASTM E1570-11 Standard practice for computed tomographic (CT) examination," Standard, ASTM International, West Conshohocken, PA.

ASTM (2015), "ASTM ISO/ASTM52900-15 Standard terminology for additive manufacturing – general principles – terminology," Standard, ASTM International, West Conshohocken, PA.

Baddeley, A.J., Moyeed, R.A., Howard, C.V. and Boyde, A. (1993), "Analysis of a three-dimensional point pattern with replication," *Journal of the Royal Statistical Society. Series C (Applied Statistics)*, Vol. 42 No. 4, pp. 641–668.

Berretta, S., Evans, K. and Ghita, O. (2015), "Processability of PEEK, a new polymer for high temperature laser sintering (HT-LS)," *European Polymer Journal*, Vol. 68, pp. 243–266.

Brugo, T., Palazzetti, R., Ciric-Kostic, S., Yan, X., Minak, G. and Zucchelli, A. (2016), "Fracture mechanics of laser sintered cracked polyamide for a new method to induce cracks by additive manufacturing," *Polymer Testing*, Vol. 50, pp. 301–308.

Bruker (2018), "Morphometric parameters measured by skyscan ct-analyser software," available at: `http://bruker-microct.com/next/CTAn03.pdf`, (accessed 20 September 2018).

Chiffre, L.D., Carmignato, S., Kruth, J.P., Schmitt, R. and Weckenmann, A. (2014), "Industrial applications of computed tomography," *CIRP Annals*, Vol. 63 No. 2, pp. 655–677.

Chlebus, E., Kuźnicka, B., Dziedzic, R. and Kurzynowski, T. (2015), "Titanium alloyed with rhenium by selective laser melting," *Materials Science and Engineering: A*, Vol. 620, pp. 155–163.

Dewulf, W., Pavan, M., Craeghs, T. and Kruth, J.P. (2016), "Using x-ray computed tomography to improve the porosity level of polyamide-12 laser sintered parts," *CIRP Annals*, Vol. 65 No. 1, pp. 205–208.

du Plessis, A. and le Roux, S.G. (2018), "Standardized x-ray tomography testing of additively manufactured parts: A round robin test," *Additive Manufacturing*, Vol. 24, pp. 125–136.

du Plessis, A., le Roux, S.G. and Steyn, F. (2015), "X-ray computed tomography of consumer-grade 3d-printed parts," *3D Printing and Additive Manufacturing*, Vol. 2 No. 4, pp. 190–195.

du Plessis, A., le Roux, S.G. and Steyn, F. (2016), "Quality investigation of 3d printer filament using laboratory x-ray tomography," *3D Printing and Additive Manufacturing*, Vol. 3 No. 4, pp. 262–267.

du Plessis, A., Yadroitsev, I., Yadroitsava, I. and Le Roux, S.G. (2018), "X-ray microcomputed tomography in additive manufacturing: A review of the current technology and applications," *3D Printing and Additive Manufacturing*, Vol. 5 No. 3, pp. 227–247.

Dupin, S., Lame, O., Barrès, C. and Charmeau, J.Y. (2012), "Microstructural origin of physical and mechanical properties of polyamide 12 processed by laser sintering," *European Polymer Journal*, Vol. 48 No. 9, pp. 1611–1621.

Dzogbewu, T., Du Plessis, A., Yadroitsev, I., Krakhmalev, P. and Yadroitsava, I. (2017), "Optimal process parameters for in situ alloyed Ti15Mo structures by laser powder bed fusion," in *Proceedings of 28th SFF Symposium*, pp. 75–96.

Ghita, O., James, E., Trimble, R. and Evans, K. (2014), "Physico-chemical behaviour of poly (ether ketone) (PEK) in high temperature laser sintering (HT-LS)," *Journal of Materials Processing Technology*, Vol. 214 No. 4, pp. 969–978.

Goodridge, R.D., Tuck, C.J. and Hague, R.J.M. (2012), "Laser sintering of polyamides and other polymers," *Progress in Materials Science*, Vol. 57 No. 2, pp. 229–267.

Jansson, A. and Pejryd, L. (2016), "Characterisation of carbon fibre-reinforced polyamide manufactured by selective laser sintering," *Additive Manufacturing*, Vol. 9, pp. 7–13.

Jones, A.C., Arns, C.H., Hutmacher, D.W., Milthorpe, B.K., Sheppard, A.P. and Knackstedt, M.A. (2009), "The correlation of pore morphology, interconnectivity and physical properties of 3d ceramic scaffolds with bone ingrowth," *Biomaterials*, Vol. 30 No. 7, pp. 1440–1451.

Kruth, J.P., Levy, G., Klocke, F. and Childs, T. (2007), "Consolidation phenomena in laser and powder-bed based layered manufacturing," *CIRP Annals-Manufacturing Technology*, Vol. 56 No. 2, pp. 730–759.

Lorensen, W.E. and Cline, H.E. (1987), "Marching cubes: A high resolution 3D surface construction algorithm," *SIGGRAPH Comput. Graph.*, Vol. 21 No. 4, pp. 163–169.

Meyers, M. and Chawla, K. (2009), "Fracture: Macroscopic aspects," in *Mechanical behavior of materials*, Cambridge University Press, Cambridge; New York, 2nd edn., pp. 404–465.

Pavan, M., Craeghs, T., Kruth, J.P. and Dewulf, W. (2018), "Investigating the influence of x-ray CT parameters on porosity measurement of laser sintered PA12 parts using a design-of-experiment approach," *Polymer Testing*, Vol. 66, pp. 203–212.

Pavan, M., Craeghs, T., Verhelst, R., Ducatteeuw, O., Kruth, J.P. and Dewulf, W. (2016), "CT-based quality control of laser sintering of polymers," *Case Studies in Nondestructive Testing and Evaluation*, Vol. 6, pp. 62–68, special Issue: Industrial computed tomography.

Pavan, M., Faes, M., Strobbe, D., Hooreweder, B.V., Craeghs, T., Moens, D. and Dewulf, W. (2017), "On the influence of interlayer time and energy density on selected critical-to-quality properties of PA12 parts produced via laser sintering," *Polymer Testing*, Vol. 61, pp. 386–395.

Rouholamin, D. and Hopkinson, N. (2014), "An investigation on the suitability of micro-computed tomography as a non-destructive technique to assess the morphology of laser sintered nylon 12 parts," *Proceedings of the Institution of Mechanical Engineers, Part B: Journal of Engineering Manufacture*, Vol. 228 No. 12, pp. 1529–1542.

Rüsenberg, S., Schmidt, L. and Schmid, H.J. (2011), "Mechanical and physical properties – a way to assess quality of laser sintered parts," in *Proceedings of 22th SFF Symposium*, pp. 239–251.

Schmidt, M., Merklein, M., Bourell, D., Dimitrov, D., Hausotte, T., Wegener, K., Overmeyer, L., Vollertsen, F. and Levy, G.N. (2017), "Laser based additive manufacturing in industry and academia," *CIRP Annals*, Vol. 66 No. 2, pp. 561–583.

Stichel, T., Frick, T., Laumer, T., Tenner, F., Hausotte, T., Merklein, M. and Schmidt, M. (2018), "A round robin study for selective laser sintering of polymers: Back tracing of the pore morphology to the process parameters," *Journal of Materials Processing Technology*, Vol. 252, pp. 537–545.

Thompson, A., Maskery, I. and Leach, R.K. (2016), "X-ray computed tomography for additive manufacturing: a review," *Measurement Science and Technology*, Vol. 27 No. 7, p. 072001.

Wohlers, T.T., Campbell, I., Diegel, O. and Kowen, J. (2018a), "Final part production," in *Wohlers Report 2018: 3D printing and Additive Manufacturing State of the Industry Annual Worldwide Progress Report*, Wohlers Associates, Fort Collins, pp. 173–227.

Wohlers, T.T., Campbell, I., Diegel, O. and Kowen, J. (2018b), "Materials and processes," in *Wohlers Report 2018: 3D printing and Additive Manufacturing State of the Industry Annual Worldwide Progress Report*, Wohlers Associates, Fort Collins, pp. 34–63.